Article

A van der Waals Density Functional Study of MoO and Its Oxygen Vacancies

Katherine Inzani, Tor Grande, Fride Vullum-Bruer, and Sverre Magnus Selbach

J. Phys. Chem. C, **Just Accepted Manuscript** • DOI: 10.1021/acs.jpcc.6b00585 • Publication Date (Web): 08 Apr 2016

A van der Waals Density Functional Study of MoO_3 and its Oxygen Vacancies

*Katherine Inzani, Tor Grande, Fride Vullum-Bruer and Sverre M. Selbach**

Department of Materials Science and Engineering, Norwegian University of Science and Technology, N-7491 Trondheim, Norway

ABSTRACT

The electronic structure of layered molybdenum trioxide MoO_3 is highly sensitive to changes in oxygen stoichiometry as Mo^{6+} has an empty 4*d* shell. Applications of MoO_3 are responsive to small changes in vacancy concentration, with some functions relying on a narrow window of oxygen non-stoichiometry. Difficulties in analyzing the energetics of oxygen vacancies by computational methods stem from the inability to accurately model the layered structure of MoO_3. One unit cell parameter is governed by long range forces across the structural gaps and these dispersed interactions are not well described by conventional density functional theory (DFT) methods. With the exchange functional vdW-DF2 we accurately model the structure, in good agreement with experimental data. This basis allows exploration of the effect of oxygen non-stoichiometry on the electronic structure and properties of the oxygen deficient material. The layered structure efficiently screens the structural perturbations caused by oxygen vacancies. The enthalpies of formation are calculated for oxygen vacancies at the three symmetry inequivalent oxygen sites. The oxygen deficiency in MoO_3 gives rise to Mo 4*d* gap states with energy levels dependent on the type of oxygen vacancy.

INTRODUCTION

Transition metal oxides are known for their remarkable optical and electrical properties with wide-ranging conductive and magnetic characteristics resulting from partially filled cation d-shells. Molybdenum trioxide (MoO_3) is notable for its photo-, gaso-, thermo- and electro-chromism, high catalytic activity and variable band gap.[1–7] In stoichiometric MoO_3 the Mo^{6+} cation has an empty 4*d* shell, however, the material is stable, and often utilized, in an oxygen deficient state. Oxygen vacancies donate electrons to the Mo 4*d* states, which are responsible for many desirable and a few detrimental characteristics of the material.[8–10] As oxygen vacancies play an important role in MoO_3, understanding the effect of oxygen vacancies on the structural and electronic properties is imperative to the majority of applications. In addition, MoO_3 is in the family of inorganic layered compounds held together by weak nonlocal forces, into which there is a growing body of research. Inclusion of nonlocal bonding in the computation of MoO_3 helps with the description of anisotropic bulk properties as well as supporting the use of two-dimensional sheets, belts and flakes in many electronic devices.[10–15]

The thermodynamically stable phase of MoO_3 is a unique orthorhombic layered structure (Figure 1), space group *Pbnm*, with each layer comprising two sub-layers of MoO_6 distorted octahedra, edge-sharing along the *c*-axis and corner-sharing along the *a*-axis. The layers are bound by weak, mainly van der Waals, interactions and the separation between the layers is known as the *van der Waals gap*. There are three unique oxygen positions, O1 – singly coordinated by a double-bond to the molybdenum atom, apical on the octahedron; O2 – doubly coordinated and asymmetrically bridging the corner-sharing of the octahedra; and O3 – which is triply coordinated and symmetrically bridges the edge-sharing.

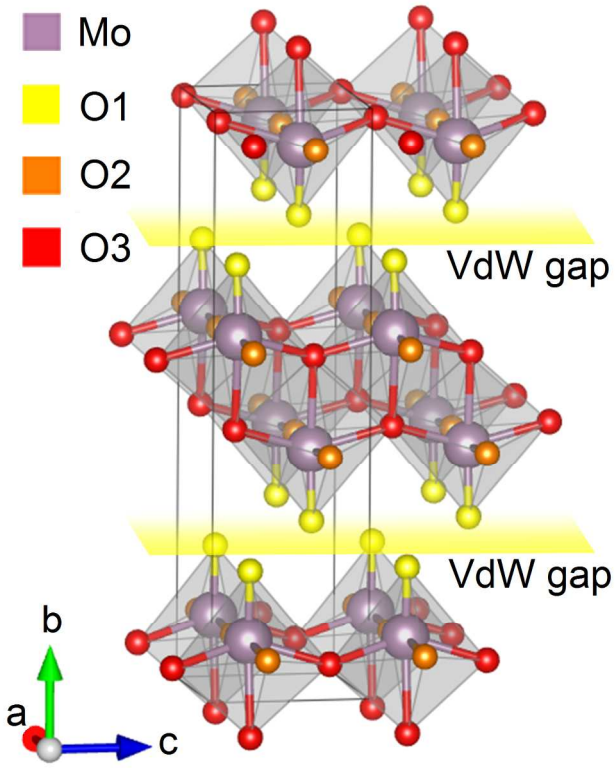

Figure 1. Crystal structure of MoO_3 showing the three inequivalent oxygen positions and the van der Waals gap. O1 is the apical oxygen; O2 is corner-sharing and O3 edge-sharing.

Stoichiometric MoO_3 is a wide-gap semiconductor with a band gap of 3.2 eV and a $4d^0$ electron configuration.[16] The conduction band minimum (CBM) is composed primarily of empty Mo 4*d* states and the valence band maximum (VBM) of O 2*p* states. Oxygen vacancies both donate electrons to the Mo 4*d* states and reduce the crystal field sufficiently to allow the formation of extended 4*d* gap states.[17]

Photovoltaics is a rapidly growing technological field and one in which MoO_3 has found several niches, being used as an electron injection layer in organic solar cells and gaining interest as an absorbing material in new generations of solar cells.[9,18–22] Due to the importance of energy level alignment, interband transitions and optical properties in photovoltaic applications, awareness of the effect of oxygen non-stoichiometry on the electronic structure of MoO_3 is

imperative for design of high-efficiency devices. Vacancy induced band gap states in MoO_3 have been utilized for sub-band gap transitions and enhancement of solar cell device performance.[10,19,21] Critical for operation, the stability of oxygen defects was found to be dependent on the method of reduction, due to differences in bonding dependent on position in the structure.[9] The bonding types were examined in the context of surface reconstruction in a theoretical study by Coquet *et al.* on slab models.[23] Related theoretical works have looked at lattice distortions, doping and electronic structure effects in MoO_3 and MoO_2, but the energetics and consequences of oxygen vacancy formation in MoO_3 has not been studied in detail.[24–27] One reason for this may be the challenges of modelling the layered structure accurately due to weak interactions between the layers, necessitating the use of surface models or artificially constrained lattice parameters. The development of van der Waals exchange correlation functionals in density functional theory (DFT) enables a self-consistent treatment of the dispersive interactions and lately these have proven useful in dealing with the layered structure of MoO_3.[24,28–30] Where past studies have been restricted by cluster or slab models, in this study we apply exchange functionals used with the van der Waals density functional vdW-DF to stoichiometric MoO_3. In addition, the DFT+U method is used to reproduce the experimentally observed gap states arising from oxygen deficiency. We compare the energetics of symmetry inequivalent vacancies in MoO_3, finding the defects to have similar and very small energies of formation, and elucidate the effect on the ionic and electronic structure.

COMPUTATIONAL DETAILS

DFT calculations were performed using the Vienna *ab initio* Simulation Package (VASP) with the projector augmented wave (PAW) pseudopotentials Mo_sv ($4s^2 4p^6 5s^1 4d^5$) and O_h ($2s^2 2p^4$).[31–34] Due to the dispersion interaction between the layers of the structure, the vdW-DF

approach was taken and the unit cell was optimized based on testing various exchange functionals used with vdW-DF. The functionals perform optimally for the hard oxygen pseudopotential supplied with VASP. Convergence was reached for an energy cut-off for the plane-wave basis set of 810 eV. For a 2x1x2 supercell a 4x2x4 Gamma centred k-point grid was used for Brillouin zone integration, with equivalent k-point density used for larger supercells. All considered structures were fully optimized until the residual forces on the ions were less than 0.01 eV for stoichiometric cells and less than 0.05 eV for defect cells. The DFT + U approach of Dudarev *et al.* was applied in addition to the vdW-DF method to better describe the energy levels of the Mo 4*d* orbitals.[35]

RESULTS

Stoichiometric MoO_3. The structure of MoO_3 includes mixed ionic-covalent bonds within the layers of octahedra and mixed electrostatic and van der Waals bonding between the layers.[36] The latter are dispersed interactions and are not well described by traditional DFT, which uses local or semi-local functionals. The exchange functionals used with vdW-DF aim to approximate non-local forces with the exchange-correlation energy taking the form of

$$E_{xc} = E_x^{GGA} + E_c^{LDA} + E_c^{nl}$$

where E_x^{GGA} is the exchange energy taken from the generalized gradient approximation (GGA), E_c^{LDA} is the correlation energy from the local density approximation (LDA) and the E_c^{nl} energy term is an addition of the non-local correlation effects.[37] The five vdW-DF exchange correlation functionals vdW-DF,[37] vdW-DF2,[38] vdW-DF-optPBE,[28] vdW-DF-optB88[28] and vdW-DF-optB86b[29] were tested for MoO_3 along with LDA and GGA. The geometry was fully optimized and the resulting lattice parameters and band gaps are compared with experimental values in Table 1.

Table 1. Lattice parameters, band gap, E_g, and interlayer spacings, *d*, calculated with different functionals.

	a [Å]	Δ*a* [%]	*b* [Å]	Δ*b* [%]	*c* [Å]	Δ*c* [%]	E_g [eV]	ΔE_g [%]	*d* [Å]
Experimental	3.963	-	13.855	-	3.696	-	3.2	-	6.928
GGA	3.927	-0.9	14.191	2.4	3.687	-0.2	1.943	-39.3	7.096
vdW-DF	3.993	0.8	14.069	1.5	3.710	0.4	2.163	-32.4	7.034
vdW-DF2	3.976	0.3	13.876	0.1	3.743	1.3	1.870	-41.6	6.938
vdW-DF-optPBE	3.929	-0.9	13.710	-1.0	3.704	0.2	1.944	-39.3	6.855
vdW-DF-optB88	3.888	-1.9	13.345	-3.7	3.707	0.3	1.760	-45.0	6.673
vdW-DF-optB86b	3.879	-2.1	13.301	-4.0	3.699	0.1	1.796	-43.9	6.650
LDA	3.799	-4.1	13.005	-6.1	3.669	-0.7	1.467	-54.2	6.503
$T \rightarrow 0$ K, ZPEC	3.957(1)	-	13.744(4)	-	3.699(1)	-			6.872

Δ is the deviation from experimental values.[16,39] $T \rightarrow 0$ K, ZPEC is the lattice parameters corrected for thermal expansion and zero point anharmonic expansion.[40]

In addition, the experimental lattice parameters with thermal expansion and zero point anharmonic expansion corrected to 0 K as calculated in Ref. 40 are shown. The functionals vdW-DF2 and vdW-DF-optPBE give the best match to the lattice parameter across the van der Waals gap, *b*. vdW-DF2 is slightly underbinding and -optPBE slightly overbinding but both are below 1 % deviation compared to both original and 0 K corrected lattice parameters. There is underbinding when GGA and vdW-DF are used, consistent with results for other van der Waals systems.[41] However, -optB88 and -optB86b have previously performed better on layered crystal structures than vdW-DF2 and -optPBE.[41] The atypical response of this system could be due to the rich combination of bonding contributions, making MoO_3 a remarkable case. Indeed, a comparison study of the two layered molybdenum compounds MoO_3 and MoS_2 found that MoO_3

could not be as accurately described by the vdW-DF approach as MoS_2.[42] Continuing on this assumption that MoO_3 is unusual for a van der Waals structure, some explanation can be given by considering the repulsive forces at short separations. These have been shown to be important for transition metals, in contrast to the long range separations generally dominating in van der Waals systems.[43–46] The order of the functionals in the table follows the gradient of the exchange enhancement factor (F_x) with small reduced density gradients (s), $s < 1$, included in the models, being steep for GGA and vdW-DF and flat for LDA.[29] Looking at lattice constant b, the length decreases going down the table, suggesting a correlation with F_x at small s. The same trend from vdW-DF to LDA can be seen with the a parameter, in which direction the octahedra are corner-sharing, giving some flexibility in ionic positions. In the c direction where the octahedra are edge-sharing, giving more rigid ion positions, there is no clear trend with the various functionals and all give a reasonable approximation. Thus, it seems that the short range forces may be dominating the binding of the structure. There is support for this view from previous studies which have found that variations in binding amongst layered structures comes from covalent bonding rather than van der Waals components, and that the transition metal species strongly affects the binding energy difference between compounds.[11] Based on these observations, both the vdW-DF2 and vdW-DF-optPBE treatment of non-local forces can be used for good approximations of lattice constants for the MoO_3 structure.

The electronic band gap is typically underestimated by around 40% with the local density approximation (LDA).[47] Here, all functionals gave a significant underestimation of the band gap, with LDA being the furthest off at 54.2% deviation from the experimental value, whilst the vdW-DF functional came closest with only 32.4% deviation. The differences in band gap are mainly an indirect effect of the choice of functional and can largely be attributed to the change in

geometry. For instance, LDA produces an increased band gap of 1.76 eV when used with the geometry relaxed by vdW-DF2. While hybrid functionals can accurately predict the band gap, they do not treat the van der Waals interactions which are imperative to the cohesion of the MoO_3 structure. This leads to deviation from the lattice parameters, even when van der Waals interactions are included.[42] Due to its accurate description of the unique crystal structure of MoO_3, the vdW-DF2 functional was chosen to continue the investigation into oxygen vacancies.

As the vdW-DF method cannot account for the strong correlation between Mo 4*d* electrons which charge compensate an oxygen vacancy in a neutral cell, the DFT + U approach of Dudarev *et al.* was applied to the molybdenum 4*d* orbitals.[35] Determination of U for molybdenum oxides is not straightforward.[48–51] The fully *ab initio* linear-response approach was found to breakdown for early transition metal oxides including MoO_2.[51] Calibration with empirical data has struggled due to the empty 4*d* orbitals in MoO_3, resulting in a limited response to U on lattice parameters and band gap width.[48,49] A thermochemical basis has been used previously in which a high U of 8.6 eV was chosen.[50] However the authors later question the validity of this due to the error introduced by calculation of the O_2 molecule needed to fulfill the thermodynamic relations.[49] In addition, empirical comparisons are hampered in these cases by poor treatment of van der Waals interactions by GGA exchange functionals, exhibited by overestimation of lattice parameters.[49,50] This will correspond to underestimation of thermodynamic quantities such as absorption energies, and using these as a basis will lead to a severe choice of U that may not reflect the electronic structure. Despite this, a strong electron correlation is still expected in MoO_3. A study by Coquet *et al.* based on charge localization analysis of reduced Mo centers by a hybrid DFT cluster model found strong correlation of 4*d* electrons replicated by $U = 6.3$ eV.[23] Use of hybrid DFT functionals is unsuitable here due to the

large supercells necessary to isolate a vacancy. However, the issues with empirical treatment can be somewhat avoided in the non-stoichiometric case as the U correction can act directly on the 4*d* electrons. Thus, the effect of U on electronic structure can be tracked and the available experimental data makes empirical selection of U an appropriate choice here. The gap states arising from oxygen vacancies in MoO_3 lie close to the conduction band minimum (CBM). A recent report on a MoO_3 nanobelt with oxygen vacancies quantified by ultraviolet photoelectron spectroscopy (UPS) shows that the peak of the gap states occurs 1.9 eV above the valence band maximum (VBM).[10] This justifies a choice of U parameter that elicits intermediate states near the top of the band gap.

The density of states (DOS) was calculated for a range of U for the MoO_3 structure with an oxygen vacancy at the O2 position. Without using the DFT + U method the calculated Mo 4*d* states introduced by the oxygen vacancy appear high up in the conduction band, an overly delocalized estimation due to the unphysical self-interaction of *d*-electrons included in DFT.[23] The U parameter was applied to modify these states and Figure 2 displays the resulting band gap, with the VBM normalized to 0 eV for ease of comparison, and the energy positions of the stoichiometric and defect CBM and defect gap states plotted against the U value. Where the gap states are next to the CBM (for U = 3 and 3.5 eV) they are clearly distinguished in the DOS by a minimum density of zero between the states and the CBM and an area equal to two electrons, which are the two electrons donated from the oxygen vacancy.

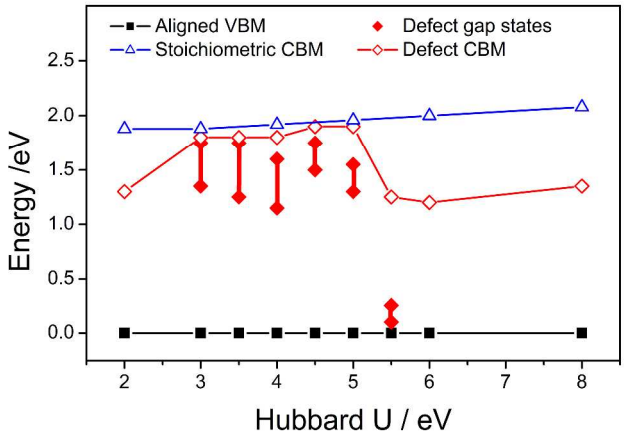

Figure 2. Aligned valence band maximum, stoichiometric conduction band minimum, defect gap states and defect conduction band minimum as a function of U parameter for a 2x1x2 supercell, where the defect is an oxygen vacancy on the O2 position.

For all values of U, defect cells have a band gap smaller than the calculated value for the stoichiometric structure. This is due to the defect deforming the octahedral geometry, causing changes in the orbital overlap, although smearing of the d-states caused by the Hubbard U term could also contribute.[24] The ordinary trend is that increasing U widens the band gap due to the occupied VBM and the unoccupied CBM being forced away from each other in energy. The situation shown in Figure 2 is complicated by the presence of occupied states within the band gap but the trends can still be understood by this tendency. The band gap does increase with U parameter up to U= 5 eV, whilst the intermediate states are consolidated and shifted deeper into the band gap. The band gap decreases from U = 5.5 eV when the occupied gap states are depressed to the VBM but continues to increase when the defect states are fully incorporated in the valence band. At U values lower and higher than 5.5 eV the intermediate states are assimilated into the conduction band and valence band respectively. A Hubbard U value of 5 eV was chosen as the most suitable because of the maximum band gap occurring at this point and

the gap state position being comparable to experimental values.[10,16] This is in keeping with the strongly correlated behaviour previously found.[23]

Oxygen vacancy formation energies. Properties of MoO_3 that originate from oxygen vacancies will be regulated by the vacancy concentration. Defect concentrations are determined by formation energies, which depend on the structural changes and the charge of the defect. The formation energy of a point defect is defined as

$$E_{\mathrm{f,def}} = E_{\mathrm{def\_cell}} - E_{\mathrm{perf\_cell}} - \sum n_i \mu_i$$

where $E_{\mathrm{def\_cell}}$ is the total energy of the defect-containing system consisting of n_i atoms, with atomic chemical potential μ_i. From this the total energy of the perfect stoichiometric cell, $E_{\mathrm{perf\_cell}}$, is subtracted with the sum over the removed species for mass balance. For a cell with charge q the expression is expanded to account for electroneutrality,

$$E_{\mathrm{f,def}} = E_{\mathrm{def\_cell}}^{\mathrm{charge}\ q} + \overset{correction}{E_{\mathrm{def\_cell}}^{\mathrm{charge}\ q}} - E_{\mathrm{perf\_cell}}$$
$$-\sum n_i \mu_i + q\left[\left(E_{\mathrm{VBM}} + \Delta v\right) + \Delta E_{\mathrm{F}}\right]$$

where the electrons in the system are described by their chemical potential which can be taken as the Fermi energy E_F measured relative to the valence band maximum E_{VBM}. The effect of artificial periodicity is accounted for by an image charge correction. In addition, the imposed cell charge must be balanced by a potential alignment term, Δv.[52,53]

There are several schemes available to do these corrections. One system applicable to anisotropic crystal structures is the method of Makov and Payne, which takes the Madelung energy, α, and the dielectric constant, ε, into account.[54] Within this model there is finite scaling of the defect formation energy with supercell size. This can be applied to correct for finite-size effects by treating neutral cells with linear extrapolation and charged cells with a second order

polynomial.[55] Taking this approach, three supercell sizes were used, 2x1x2, 2x1x3 and 3x1x3, with respectively 64, 96 and 144 atoms. The 16 atom 1x1x1 unit cell showed artificial defect-defect interactions, so it was not included for fitting. Neutral, +1 and +2 charge states were modelled for vacancies on each of the three oxygen positions in MoO_3. The upper limit for μ_O was set as zero, corresponding to gaseous oxygen in an oxygen rich environment. The lower limit was defined by the reduction scenario $MoO_2 + ½\ O_2 = MoO_3$, $\mu_O = E(MoO_3) - E(MoO_2) =$ -5.085 eV. The raw $E_{f,def}$ of neutral cells fits well to linear scaling with 1/N, N being the number of atoms in the supercell. However, the charged cells were poorly modelled by the polynomial scaling of the Makov-Payne scheme, suggesting unphysical low defect formation energies. The cause of this could be the relatively small and non-isometric sample of supercell sizes, but larger cell sizes are unfeasible with the stringent conditions of this study. Instead, a linear extrapolation fits well to the charged cells and provides corrected defect energies of formation close to the $E_{f,def}$ of the largest cell.[56] The linear fits are shown in Figure 3 for the oxidizing limit. The 3x1x3 defect energies of formation and corrected defect energies of formation for vacancies on the three oxygen positions are given in Table 2.

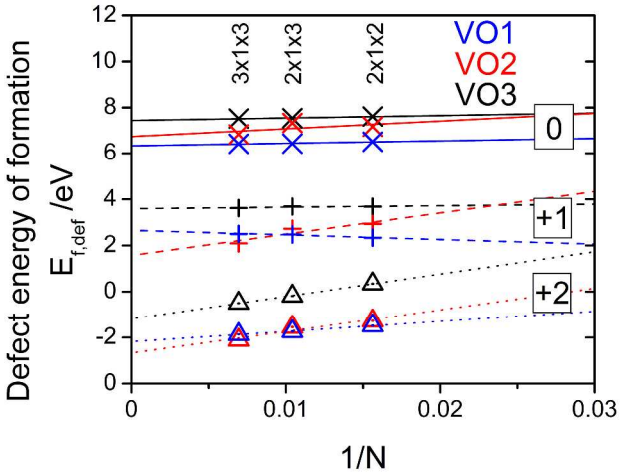

Figure 3. Defect energy of formation, $E_{f,def}$ vs. 1/N with μ_O= 0 eV, where N is the number of atoms in the supercell.

Table 2. Defect energies of formation in eV for the three oxygen vacancy positions, in 0, +1 and +2 charge states, in two oxygen atmospheres. Raw values from the 3x1x3 supercell and corrected values from linear extrapolation of supercell size are given.

		3x1x3 values		corrected values	
vacancy position	charge	O-poor μ_O=-5.085 eV	O-rich μ_O=0 eV	O-poor μ_O=-5.085 eV	O-rich μ_O=0 eV
O1	0	1.334	6.419	1.248	6.333
	+1	-2.584	2.501	-2.428	2.657
	+2	-6.944	-1.859	-7.258	-2.174
O2	0	1.742	6.827	1.651	6.735
	+1	-2.992	2.093	-3.515	1.570
	+2	-7.195	-2.110	-7.754	-2.670
O3	0	2.436	7.521	2.353	7.438
	+1	-1.463	3.622	-1.491	3.594
	+2	-5.582	-0.497	-6.267	-1.182

In the oxygen rich limit the neutral formation energies are large at all vacancy positions. The O1 vacancy position has the lowest energy of formation for neutral cells, followed by O2 and O3. This relative stability in the O1 vacancy is justified intuitively by the orientation of the O1 oxygen towards the van der Waals gap. The defect formation energies in oxygen rich conditions range from 6.3-7.4 eV for neutral cells. This is in excellent agreement with the values reported in an early work by Tokarz-Sobieraj *et al.*, where surface cluster DFT calculations gave formation

energies of 6.8-7.6 eV.[25] However, the lowest energy of formation was reported to be on the O3 position. This discrepancy is likely due to the fact that the geometry of the cluster was not optimized. This is further supported by the DFT + U work of Coquet *et al.* who calculated the stability of vacancies to follow the same order as found here.[23]

In the reducing limit the formation energies are small for neutral cells and highly negative for charged cells. This is corroborated by the ready reduction of MoO_3.[57] Furthermore, an estimation made by Gai *et al.*, based on thermodynamic relations and experimental data, predicted a low enthalpy of vacancy formation of 0.4 eV ± 0.1 eV at 298 K.[58] As this estimation is an average over a range of oxygen stoichiometries, it is logical that the values given here differ as they correspond to vacancy formation in the dilute limit. The dilute limit is quickly surpassed in MoO_{3-x} as vacancy ordering and extended defects form at low temperatures and at concentrations of oxygen vacancies as low as $x = 0.001$.[59] Such ordering increases the configurational entropy and acts to stabilize the system, increasing the energy of formation of defect formation with progressive reduction.

The different charge states of the defects are considered in Figure 4, a plot of the formation energies in both oxygen conditions as a function of the Fermi energy. For alignment the Fermi energy is set at zero at the top of the valence band, and the band gap is taken as that of the stoichiometric cell. There is a transition from the +2 state to the neutral state as we move through the band gap. There is no range of E_F where the +1 charge state is stable. These transition energies relative to the VBM are given in Table 3. The O1 vacancy has the deepest transition energy and the O2 has the shallowest.

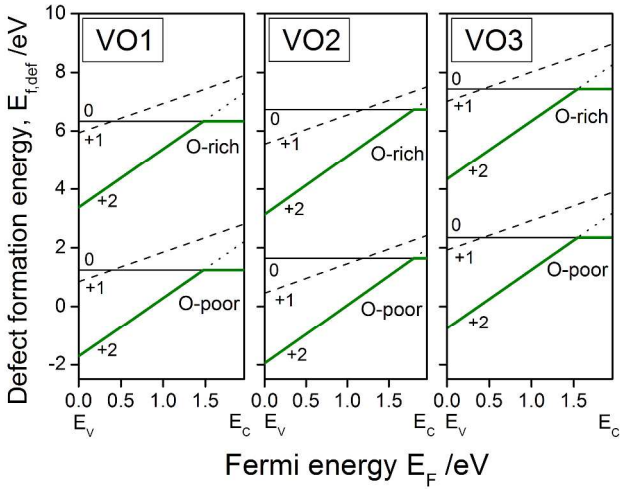

Figure 4. The formation energy of the most stable charge state (green line) of the three oxygen vacancies as a function of the Fermi energy, E_F, for oxygen rich and oxygen poor conditions.

Table 3. Transition energies in eV of the charge states of the three oxygen vacancy positions relative to the VBM.

vacancy position	+2/0
O1	1.478
O2	1.802
O3	1.548

Structural perturbations from oxygen vacancies. Relaxed ion positions around vacancies on O1, O2 and O3 positions overlaid on the unaffected, stoichiometric positions are illustrated in Figure 5, calculated in a 3x1x3 cell. The O1 and O3 vacancies cause little distortion of the surrounding ion positions compared with the O2 vacancy, which results in substantial movement of an adjacent Mo away from the vacancy and an apical O towards the vacancy. In all cases, the displacements are well confined to the layer in which the vacancy is located. The geometry

effects on the vacancy containing octahedra are examined in Figure 6, which shows Mo—O bond lengths and select bond angles compared to the stoichiometric octahedron. The O2 and O3 vacancies further distort the octahedron, whereas the O1 vacancy allows straightening of the [100] oriented bonds, from 167° to 175°, restoring some of the octahedral symmetry. The apical oxygen on both the Mo ions with an O2 and an O3 vacancy moves away from its approximate [010] alignment and towards the vacant site; in the case of vacant O2 the opposite ∠O1O2 distorts from 91° to 138° and in the case of vacant O3 the opposite ∠O3O1 distorts from 106° to 110°, both taking the geometry further away from a perfect octahedron.

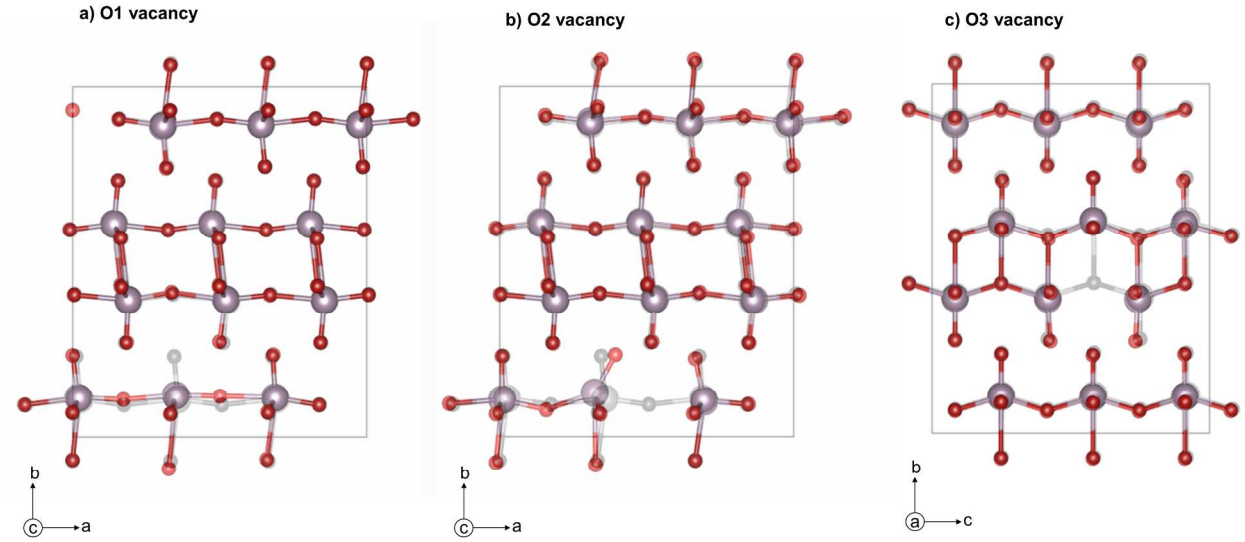

Figure 5. Relaxed structures with vacancies on positions a) O1, b) O2 and c) O3, overlaid on the stoichiometric positions.

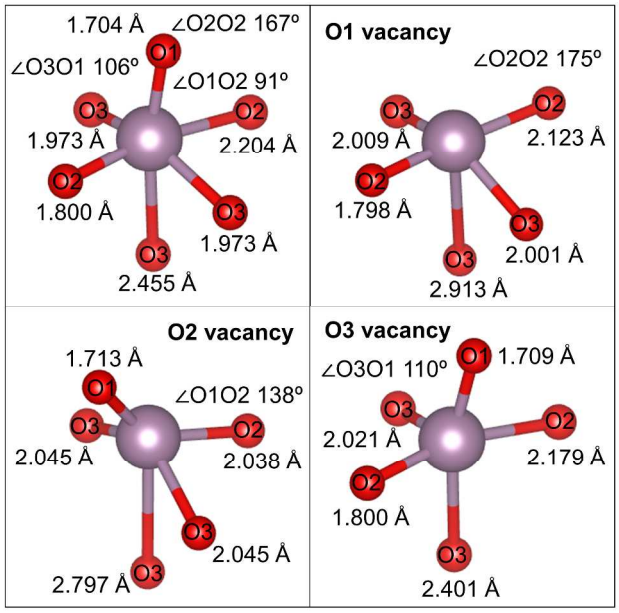

Figure 6. Bond lengths and select bond angles on an octahedron in stoichiometric MoO_3, and the distorted polyhedrons adjacent to vacancies on O1, O2, O3 positions. Octahedra are aligned to comparable orientations.

The displacements are quantified and plotted with distance from the vacant site in Figure 7. The O2 defect causes the greatest structural perturbation, causing the closest Mo ion to shift by 0.48 Å and the nearest O ions by nearly 0.3 Å, while the O1 and O3 vacancies do not cause any displacements larger than 0.2 Å. Moving away from the vacancy the ion displacement quickly declines and there are no displacements greater than 0.05 Å at a distance of 7 Å, indicating that a 2x1x2 supercell, in which the smallest cell parameter is 7.486 Å, is large enough to contain the effect of an isolated vacancy. 2x1x2 supercells are hence used for further analysis of the electronic structure. Figure 7 also differentiates ions within the same layer as the defect and those in another layer. For all three defects, the "out of layer" ions are displaced by less than 0.1 Å, so it is clear that for all three defects the displacements are well confined to the defect layer and

structural effects are screened by the lack of direct structural coupling across the van der Waals gap.

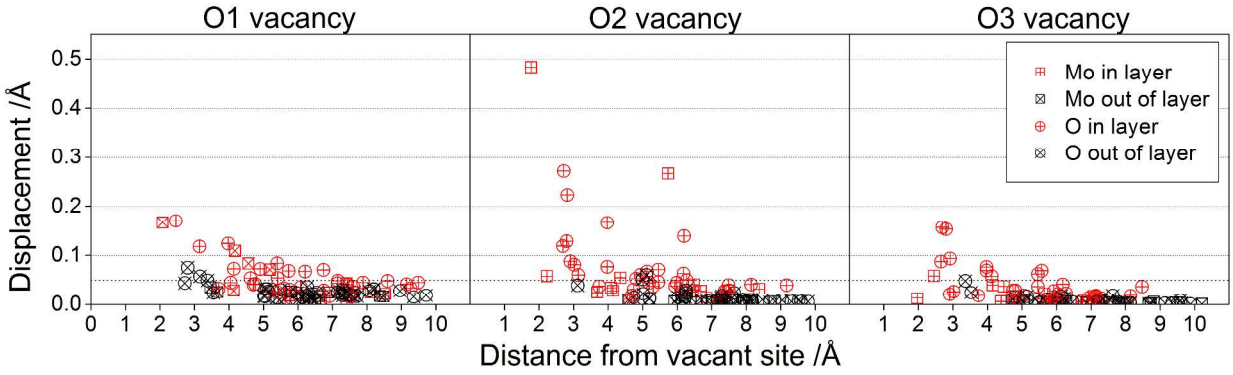

Figure 7. Mo and O ion displacements from stoichiometric position with distance from the vacant site for O1, O2 and O3 vacancy positions in a 3x1x3 (144 atom) supercell. *In layer* and *out of layer* signifies if the ion is located within the same layer as the vacancy or not.

Electronic structure. The structural effects can be further understood by comparison with the electron localization function (ELF) plots in Figure 8. The ELF is an integration of the charge density that illustrates the localization of electrons.[60] The figures show the ELF plot of a neutral cell with an oxygen vacancy, the equivalent cell with a +2 charge imposed and the stoichiometric cell from the same perspective. The neutral cell includes the electrons that remain from the vacant oxygen site, and with each defect these electrons move to fill orbitals at the nearest Mo ion whilst distorting the orbitals towards the vacant site. Electrons from the O1 vacancy are concentrated towards the van der Waals gap where there is space to leave the surrounding structure largely unaffected. In contrast, the O2 vacancy forces the Mo orbital between the remaining oxygen ions, heavily interfering with the octahedral dimensions, as shown in Figure 6. The electrons from the O3 vacancy largely remain localized at the vacant site but also contribute to the two adjacent Mo to which the oxygen was symmetrically bonded, although not to the third more distant Mo. The +2 charge state depicts the circumstance in which the charge compensating

electrons from the vacancy do not remain in its vicinity. Interestingly, in this situation the structural changes almost exactly remain for all three vacancy positions.

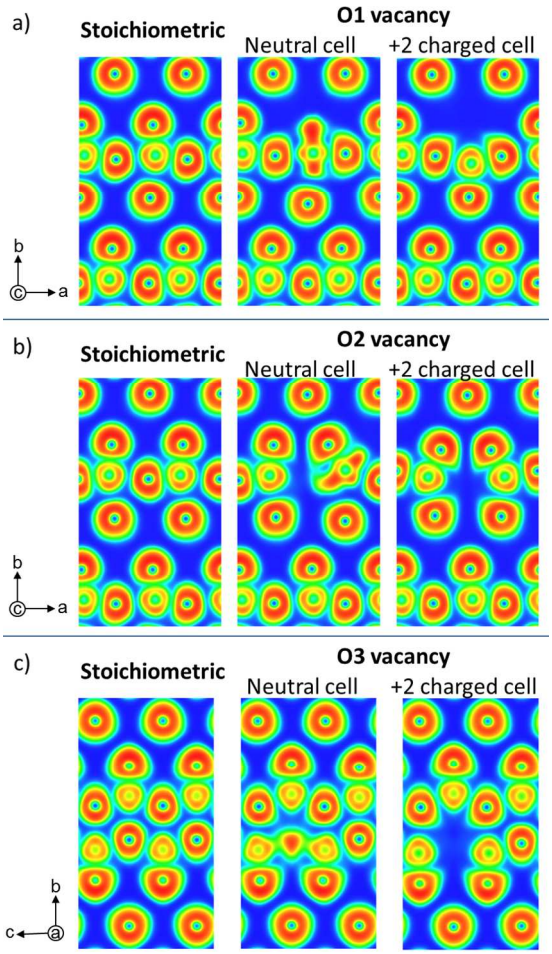

Figure 8. Plots of the electron localization function of 2x1x2 supercells containing a) O1, b) O2 and c) O3 vacancies. The defect cells are shown in neutral and +2 charge states alongside the stoichiometric cell.

The electronic effects of these charge density changes can be seen by examining the band structure and DOS, plotted alongside the stoichiometric case in Figure 9a-d, with the corresponding Brillouin zone shown in Figure 9e. The Fermi energy is set at 0 eV and the orbital occupations can be seen in the partial DOS. In the stoichiometric cell the band gap is calculated as 1.96 eV and the VBM is composed primarily of O 2*p* states and the CBM mainly of Mo 4*d*

states. The principal effect of the defect is to introduce states within the band gap. Integrating the DOS over the energy range of the gap states reveals that exactly two electrons occupy these states. This corresponds to the two electrons donated by the oxygen removed from the vacant site. The nature of the gap states differs with each vacancy position in energy level and range although they are all primarily composed of Mo 4*d* orbitals. The band structure of the gap states is sloped in directions that correspond to the c-axis, the direction of the edge-sharing octahedra, and completely flat along the b-axis, which is perpendicular to the octahedral layers, similar to the bands at the CBM and VBM. This implies that the mobility of the charge carriers is greatest in 2D within the octahedral layers and is strongly restricted across the layers by the van der Waals gap. The defect bands also vary in gradient with vacancy position, being steepest for the O3 vacancy. Comparing this to the ELF plot, the O3 defect concentrates electrons along this edge-sharing chain of octahedra and further spreads the states in energy. Another effect of the defects is to reduce the band gap, from 1.96 eV for the stoichiometric cell to 1.64, 1.88 and 1.68 eV for O1, O2 and O3 defects respectively. This effect is more pronounced for the charged cells (DOS in Figure S1), where the band gap narrows with increasing charge. Although these calculated band gap values are underestimations of the experimental values, the trend can be understood as the orbital overlap changing with octahedral distortion, as displayed in figures 5 and 6. There is additional dispersion of the gap states in the charged cells due to the effect of the U parameter on the unfilled states.

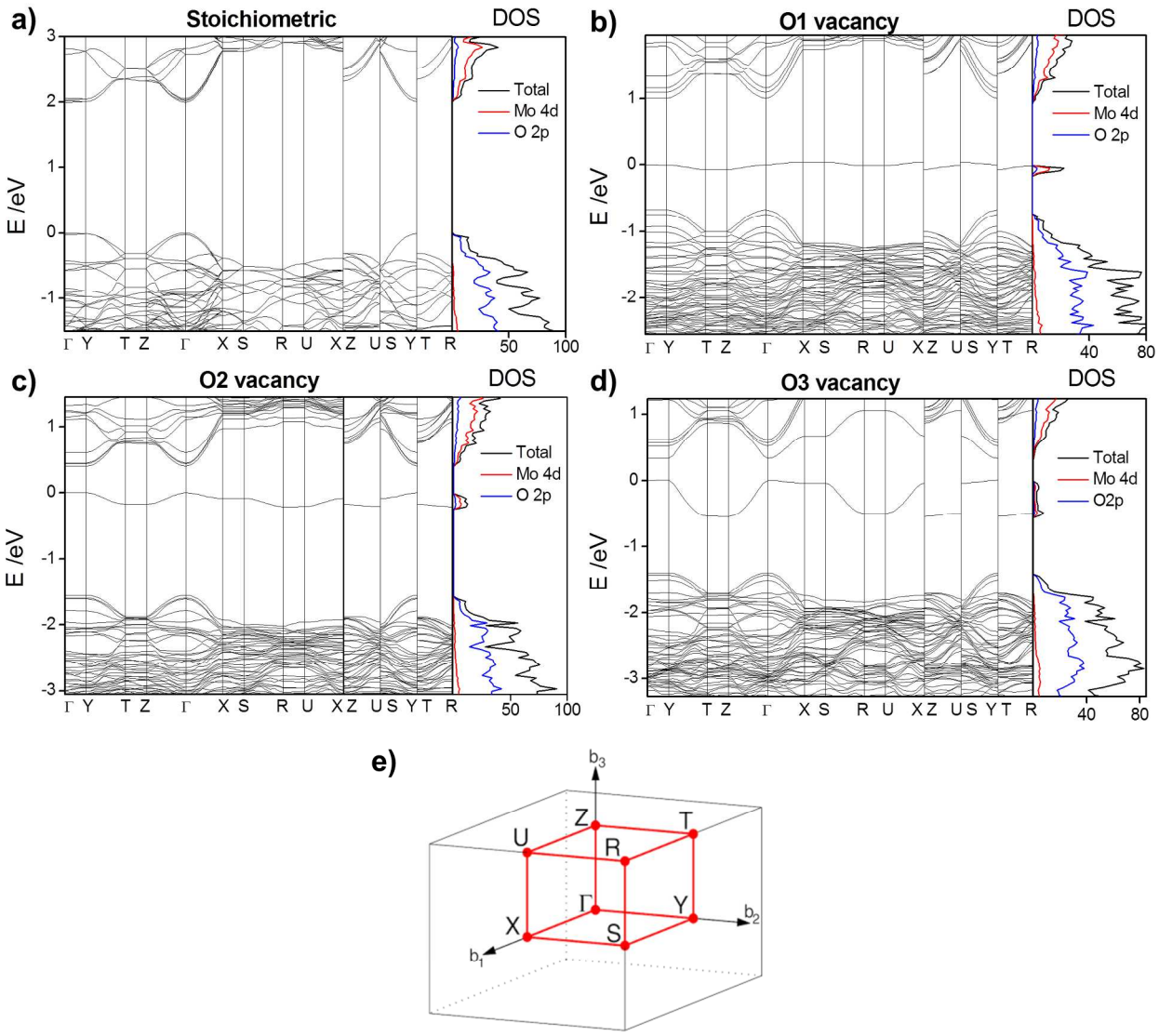

Figure 9. Band structures of MoO_3 a) in the stoichiometric case, and with a vacancy on b) O1, c) O2 and d) O3 positions, alongside the total, Mo 4*d* and O 2*p* density of states. The Fermi level is aligned to 0 eV. e) Brillouin zone of an orthorhombic lattice.[61] The path Γ-Y-T-Z-Γ-X-S-R-U-X|Z-U|S-Y|T-R was used for calculating bandstructures.

The orbitals around the Fermi level are resolved into Mo $4d_{xy}$, $4d_{yz}$, $4d_{xz}$, $4d_{x^2-y^2}$, $4d_{z^2}$ and O 2*p* orbitals in Figure 10. Despite the distorted octahedra of the structure, the effect of the crystal field is seen in the stoichiometric DOS in that the bottom of the conduction band is dominated by the Mo $4d_{xy}$, $4d_{yz}$ and $4d_{xz}$ states, i.e. those states which are not aligned with the Mo-O bonding

direction are lower in energy. The defects act to perturb the 4*d* levels, dependent on the changes in the octahedral symmetry. In the case of the O1 vacancy Figure 5a shows that the octahedral distortion is reduced by the vacancy as the bonds are straightened. It follows that the gap states are entirely composed of Mo $4d_{x^2-y^2}$ and $4d_{z^2}$ states, as transfer of electrons from the oxygen to the metal is most efficient for those levels pointing directly to the vacant oxygen, in the b-direction, and these electrons are distributed towards the neighbouring oxygen ions. This can be seen in the ELF plot in Figure 8a, as the electrons are concentrated in the [010] axis of the deficient octahedron and also extend into the corner-sharing [100] chain. The O2 gap states have a mixture of d_{xy} and d_{z^2} components, with electron concentration clearly distorted as displayed in the off-axis charge density in Figure 8b. Similarly, the O3 gap states have mixing of the d_{yz}, d_{xz} and d_{z^2} orbitals, alluding to the greater distortion of the octahedron seen in the geometrical changes and charge density concentrated in all z-components, seen in Figure 8c in the edge-sharing chain which zigzags in the [001] direction.

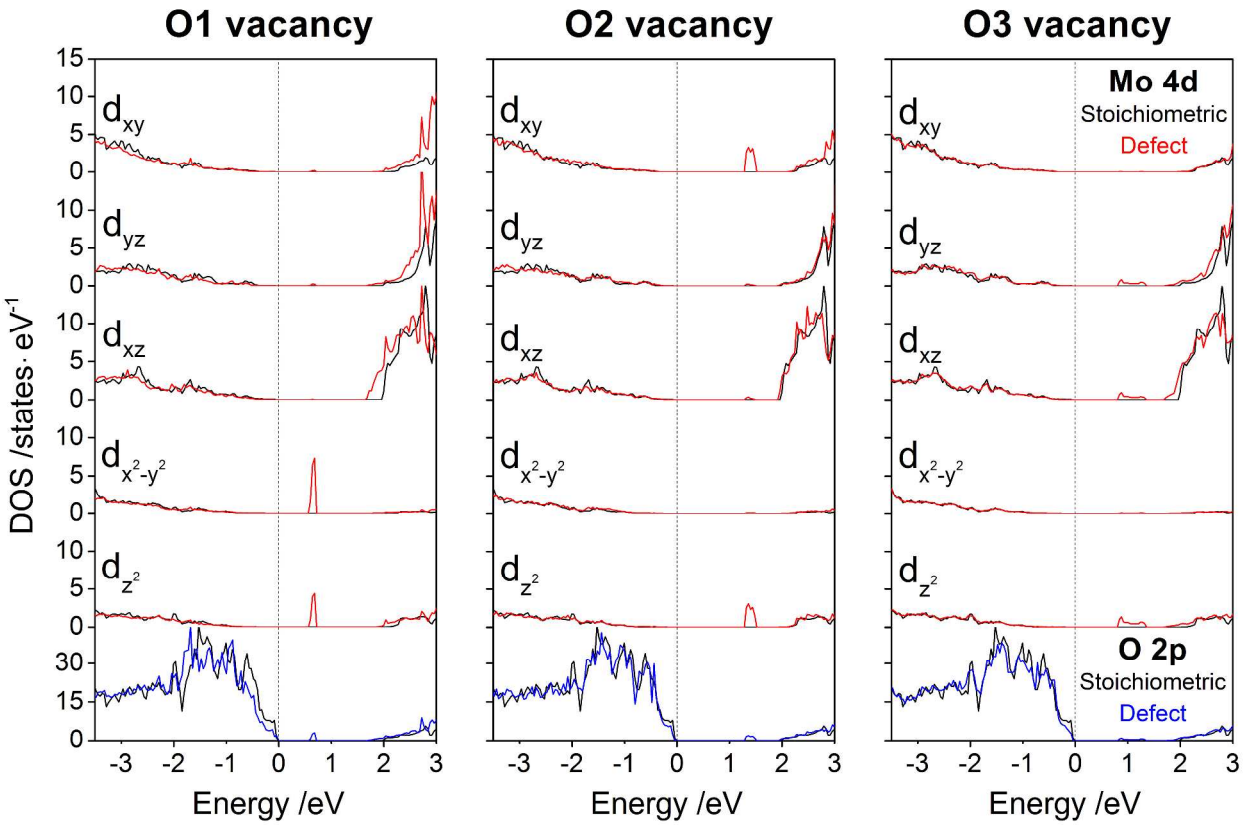

Figure 10. Orbital resolved density of states comparing the stoichiometric and defect Mo $4d_{xy}$, $4d_{yz}$, $4d_{xz}$, $4d_{x^2-y^2}$, $4d_{z^2}$ and O $2p$ orbitals, with O1, O2 and O3 vacancies.

CONCLUSIONS

The vdW-DF method provides an improved treatment of the van der Waals gap in the structure of MoO_3, and the vdW-DF2 functional can reproduce the experimental lattice parameter across the gap within 0.1%. The Dudarev DFT + U method was used to treat the Mo 4*d* orbitals, with U = 5 eV chosen based on available experimental results. The difference in formation energies of the three inequivalent oxygen vacancy positions shows that the apical, van der Waals gap-facing oxygen is the most readily removed. Calculations with charged cells revealed deep lying transition energies. Calculations of the electron localization function, band structure and density of states showed that oxygen vacancies give rise to Mo 4*d* gap states where the orbital

contributions depend on the localization of the vacancy and the octahedral distortion and orientation. The O1 vacancy reduced the initial octahedral distortion, resulting in gap states confined to the Mo $4d_{x^2-y^2}$ and $4d_{z^2}$ states, whereas the O2 and O3 vacancies deepened the octahedral distortion, giving rise to gap states with mixed Mo 4*d* components. The band structure implied an anisotropic mobility as a result of the layered structure. The band gap was reduced for all vacancy positions, however within the band gap the defect bands varied with vacancy position. The defect band was most dispersed in energy for the O3 vacancy due to the concentration of electrons along the edge-sharing chain of octahedra. The defect formation energies in oxygen rich conditions were high, from 6.3-7.4 eV, whilst the low vacancy formation energy in oxygen poor conditions explains the ready reduction of MoO_3. It should be noted that the vacancy regime of MoO_{3-x} has a narrow range of *x* for which vacancies are true point defects.[62] The situation complicates itself beyond this, as vacancies order into a superlattice. With progressive reduction the vacancies are eliminated by crystallographic shear and lattice collapse.[5] These structural changes act to stabilize the material by reducing the free energy relative to vacancies in supersaturation.

ASSOCIATED CONTENT

Supporting Information. Figure S1. Total and partial density of states of oxygen vacancies on the three oxygen positions with +1 and +2 charges. This material is available free of charge via the Internet at http://pubs.acs.org.

AUTHOR INFORMATION

Corresponding Author

*Phone: +47-73-59-40-99 ; e-mail: selbach@ntnu.no.

ACKNOWLEDGMENT

This work was performed within The Norwegian Research Centre for Solar Cell Technology project number 193829, a Centre for Environmentally-friendly Energy Research co-sponsored by the Norwegian Research Council and research and industry partners in Norway. Computational resources were provided by NOTUR, The Norwegian Metacentre for Computational Science, through the project nn9264k.

REFERENCES

(1) Fleisch, T. H.; Mains, G. J. An XPS Study of the UV Reduction and Photochromism of MoO_3 and WO_3. *J. Chem. Phys.* **1982**, *76*, 780–786.

(2) Ajito, K.; Nagahara, L. A.; Tryk, D. A.; Hashimoto, K.; Fujishima, A. Study of the Photochromic Properties of Amorphous MoO_3 Films Using Raman Microscopy. *J. Phys. Chem.* **1995**, *99*, 16383–16388.

(3) Chang, C. C.; Luo, J. Y.; Chen, T. K.; Yeh, K. W.; Huang, T. W.; Hsu, C. H.; Chao, W. H.; Ke, C. T.; Hsu, P.-C.; Wang, M. J.; *et al*. Pulsed Laser Deposition of $(MoO_3)_{1-x}(V_2O_5)_x$ Thin Films: Preparation, Characterization and Gasochromic Studies. *Thin Solid Films* **2010**, *519*, 1552–1557.

(4) Yao, D. D.; Ou, J. Z.; Latham, K.; Zhuiykov, S.; O'Mullane, A. P.; Kalantar-zadeh, K. Electrodeposited α- and ß-Phase MoO_3 Films and Investigation of Their Gasochromic Properties. *Cryst. Growth Des.* **2012**, *12*, 1865–1870.

(5) Gai-Boyes, P. L. Defects in Oxide Catalysts: Fundamental Studies of Catalysis in Action. *Catal. Rev.* **1992**, *34*, 1–54.

(6) Greiner, M. T.; Chai, L.; Helander, M. G.; Tang, W. M.; Lu, Z. H. Metal/Metal-Oxide Interfaces: How Metal Contacts Affect the Work Function and Band Structure of MoO_3. *Adv. Funct. Mater.* **2013**, *23*, 215–226.

(7) Hu, X. K.; Qian, Y. T.; Song, Z. T.; Huang, J. R.; Cao, R.; Xiao, J. Q. Comparative Study on MoO_3 and H_xMoO_3 Nanobelts: Structure and Electric Transport. *Chem. Mater.* **2008**, *20*, 1527–1533.

(8) Shi, X.-B.; Xu, M.-F.; Zhou, D.-Y.; Wang, Z.-K.; Liao, L.-S. Improved Cation Valence State in Molybdenum Oxides by Ultraviolet-Ozone Treatments and Its Applications in Organic Light-Emitting Diodes. *Appl. Phys. Lett.* **2013**, *102*, 233304.

(9) Chiam, S. Y.; Dasgupta, B.; Soler, D.; Leung, M. Y.; Liu, H.; Ooi, Z. E.; Wong, L. M.; Jiang, C. Y.; Chang, K. L.; Zhang, J. Investigating the Stability of Defects in MoO_3 and Its Role in Organic Solar Cells. *Sol. Energy Mater. Sol. Cells* **2012**, *99*, 197–203.

(10) Xiang, D.; Han, C.; Zhang, J.; Chen, W. Gap States Assisted MoO_3 Nanobelt Photodetector with Wide Spectrum Response. *Sci. Rep.* **2014**, *4*, 4891.

(11) Björkman, T.; Gulans, A.; Krasheninnikov, A. V.; Nieminen, R. M. van der Waals Bonding in Layered Compounds from Advanced Density-Functional First-Principles Calculations. *Phys. Rev. Lett.* **2012**, *108*, 235502.

(12) Berland, K.; Cooper, V. R.; Lee, K.; Schröder, E.; Thonhauser, T.; Hyldgaard, P.; Lundqvist, B. I. van der Waals Forces in Density Functional Theory: A Review of the vdW-DF Method. *Reports Prog. Phys.* **2015**, *78*, 66501.

(13) Balendhran, S.; Deng, J.; Ou, J. Z.; Walia, S.; Scott, J.; Tang, J.; Wang, K. L.; Field, M.

R.; Russo, S.; Zhuiykov, S.; *et al.* Enhanced Charge Carrier Mobility in Two-Dimensional High Dielectric Molybdenum Oxide. *Adv. Mater.* **2013**, *25*, 109–114.

(14) Hanlon, D.; Backes, C.; Higgins, T. M.; Hughes, M.; O'Neill, A.; King, P.; McEvoy, N.; Duesberg, G. S.; Mendoza Sanchez, B.; Pettersson, H.; *et al.* Production of Molybdenum Trioxide Nanosheets by Liquid Exfoliation and Their Application in High-Performance Supercapacitors. *Chem. Mater.* **2014**, *26*, 1751–1763.

(15) Alsaif, M. M. Y. a; Field, M. R.; Murdoch, B. J.; Daeneke, T.; Latham, K.; Chrimes, A. F.; Zoolfakar, A. S.; Russo, S. P.; Ou, J. Z.; Kalantar-Zadeh, K. Substoichiometric Two-Dimensional Molybdenum Oxide Flakes: A Plasmonic Gas Sensing Platform. *Nanoscale* **2014**, *6*, 12780–12791.

(16) Carcia, P. F.; McCarron, E. M. Synthesis and Properties of Thin Film Polymorphs of Molybdenum Trioxide. *Thin Solid Films* **1987**, *155*, 53–63.

(17) Werfel, F.; Minni, W. E. Photoemission Study of the Electronic Structure of Mo and Mo Oxides. *J. Phys. Chem. C* **1983**, *16*, 6091–6100.

(18) Liu, F.; Shao, S.; Guo, X.; Zhao, Y.; Xie, Z. Efficient Polymer Photovoltaic Cells Using Solution-Processed MoO_3 as Anode Buffer Layer. *Sol. Energy Mater. Sol. Cells* **2010**, *94*, 842–845.

(19) Simchi, H.; McCandless, B. E.; Meng, T.; Boyle, J. H.; Shafarman, W. N. Characterization of Reactively Sputtered Molybdenum Oxide Films for Solar Cell Application. *J. Appl. Phys.* **2013**, *114*, 013503.

(20) Jasieniak, J. J.; Seifter, J.; Jo, J.; Mates, T.; Heeger, A. J. A Solution-Processed MoO_x

Anode Interlayer for Use within Organic Photovoltaic Devices. *Adv. Funct. Mater.* **2012**, *22*, 2594–2605.

(21) Kostis, I.; Vourdas, N.; Papadimitropoulos, G.; Douvas, A.; Vasilopoulou, M.; Boukos, N.; Davazoglou, D. Effect of the Oxygen Sub-Stoichiometry and of Hydrogen Insertion on the Formation of Intermediate Bands within the Gap of Disordered Molybdenum Oxide Films. *J. Phys. Chem. C* **2013**, *117*, 18013–18020.

(22) Liang, J.; Zu, F.; Ding, L.; Xu, M.; Shi, X.; Wang, Z.; Liao, L. Aqueous Solution-Processed MoO_3 Thick Films as Hole Injection and Short-Circuit Barrier Layer in Large-Area Organic Light-Emitting Devices. *Appl. Phys. Express* **2014**, *7*, 111601.

(23) Coquet, R.; Willock, D. J. The (010) Surface of α-MoO_3, a DFT + U Study. *Phys. Chem. Chem. Phys.* **2005**, *7*, 3819–3828.

(24) Huang, P.-R.; He, Y.; Cao, C.; Lu, Z.-H. Impact of Lattice Distortion and Electron Doping on α-MoO_3 Electronic Structure. *Sci. Rep.* **2014**, *4*, 7131.

(25) Tokarz-Sobieraj, R.; Hermann, K.; Witko, M.; Blume, A.; Mestl, G.; Schlögl, R. Properties of Oxygen Sites at the MoO_3(010) Surface: Density Functional Theory Cluster Studies and Photoemission Experiments. *Surf. Sci.* **2001**, *489*, 107–125.

(26) Scanlon, D. O.; Watson, G. W.; Payne, D. J.; Atkinson, G. R.; Egdell, R. G.; Law, D. S. L. Theoretical and Experimental Study of the Electronic Structures of MoO_3 and MoO_2. *J. Phys. Chem. C* **2010**, *114*, 4636–4645.

(27) Rozzi, C. A.; Manghi, F.; Parmigiani, F. Ab Initio Fermi Surface and Conduction-Band Calculations in Oxygen-Reduced MoO_3. *Phys. Rev. B* **2003**, *68*, 75106.

(28) Klimeš, J.; Bowler, D. R.; Michaelides, A. Chemical Accuracy for the van der Waals Density Functional. *J. Phys. Condens. Matter* **2010**, *22*, 022201.

(29) Klimeš, J.; Bowler, D. R.; Michaelides, A. van der Waals Density Functionals Applied to Solids. *Phys. Rev. B* **2011**, *83*, 195131.

(30) Ding, H.; Ray, K. G.; Ozolins, V.; Asta, M. Structural and Vibrational Properties of α-MoO_3 from van der Waals Corrected Density Functional Theory Calculations. *Phys. Rev. B* **2012**, *85*, 12104.

(31) Kresse, G.; Hafner, J. Ab Initio Molecular Dynamics for Liquid Metals. *Phys. Rev. B* **1993**, *47*, 558–561.

(32) Kresse, G.; Furthmüller, J. Efficiency of Ab Initio Total Energy Calculations for Metals and Semiconductors Using a Plane-Wave Basis Set. *Comput. Mater. Sci.* **1996**, *6*, 15–50.

(33) Kresse, G.; Furthmüller, J. Efficient Iterative Schemes for Ab Initio Total-Energy Calculations Using a Plane-Wave Basis Set. *Phys. Rev. B* **1996**, *54*, 11169–11186.

(34) Kresse, G.; Joubert, D. From Ultrasoft Pseudopotentials to the Projector Augmented-Wave Method. *Phys. Rev. B* **1999**, *59*, 1758–1775.

(35) Dudarev, S. L.; Savrasov, S. Y.; Humphreys, C. J.; Sutton, A. P. Electron-Energy-Loss Spectra and the Structural Stability of Nickel Oxide: An LSDA+U Study. *Phys. Rev. B* **1998**, *57*, 1505–1509.

(36) Sayede, A. D.; Amriou, T.; Pernisek, M.; Khelifa, B.; Mathieu, C. An Ab Initio LAPW Study of the α and β Phases of Bulk Molybdenum Trioxide, MoO_3. *Chem. Phys.* **2005**, *316*, 72–82.

(37) Dion, M.; Rydberg, H.; Schröder, E.; Langreth, D. C.; Lundqvist, B. I. van der Waals Density Functional for General Geometries. *Phys. Rev. Lett.* **2004**, *92*, 246401.

(38) Lee, K.; Murray, É. D.; Kong, L.; Lundqvist, B. I.; Langreth, D. C. A Higher-Accuracy van der Waals Density Functional. *Phys. Rev. B* **2010**, *82*, 081101.

(39) Kihlborg, L. Least Squares Refinement of the Crystal Structure of Molybdenum Trioxide. *Ark. Kemi* **1963**, *21*, 357–364.

(40) Negishi, H.; Negishi, S.; Kuroiwa, Y.; Sato, N.; Aoyagi, S. Anisotropic Thermal Expansion of Layered MoO_3 Crystals. *Phys. Rev. B* **2004**, *69*, 064111.

(41) Björkman, T. Testing Several Recent van der Waals Density Functionals for Layered Structures. *J. Chem. Phys.* **2014**, *141*, 074708.

(42) Peelaers, H.; Van de Walle, C. G. First-Principles Study of van der Waals Interactions in MoS_2 and MoO_3. *J. Phys. Condens. Matter* **2014**, *26*, 305502.

(43) Wesolowski, T. A.; Parisel, O.; Ellinger, Y.; Weber, J. Comparative Study of Benzene···X (X = O_2, N_2, CO) Complexes Using Density Functional Theory: The Importance of an Accurate Exchange-Correlation Energy Density at High Reduced Density Gradients. *J. Phys. Chem. A* **1997**, *101*, 7818–7825.

(44) Zhang, Y.; Pan, W.; Yang, W. Describing van der Waals Interaction in Diatomic Molecules with Generalized Gradient Approximations: The Role of the Exchange Functional. *J. Chem. Phys.* **1997**, *107*, 7921.

(45) Csonka, G. I.; Perdew, J. P.; Ruzsinszky, A.; Philipsen, P. H. T.; Lebègue, S.; Paier, J.; Vydrov, O. A.; Ángyán, J. G. Assessing the Performance of Recent Density Functionals

for Bulk Solids. *Phys. Rev. B* **2009**, *79*, 155107.

(46) Haas, P.; Tran, F.; Blaha, P.; Schwarz, K.; Laskowski, R. Insight into the Performance of GGA Functionals for Solid-State Calculations. *Phys. Rev. B* **2009**, *80*, 195109.

(47) Perdew, J. P. Density Functional Theory and the Band Gap Problem. *Int. J. Quantum Chem. Quantum Chem. Symp.* **1986**, *19*, 497–523.

(48) Sha, X.; Chen, L.; Cooper, A. C.; Pez, G. P.; Cheng, H. Hydrogen Absorption and Diffusion in Bulk α-MoO_3. *J. Phys. Chem. C* **2009**, *113*, 11399–11407.

(49) Getsoian, A. B.; Bell, A. T. The Influence of Functionals on Density Functional Theory Calculations of the Properties of Reducible Transition Metal Oxide Catalysts. *J. Phys. Chem. C* **2013**, *117*, 25562–25578.

(50) Lutfalla, S.; Shapovalov, V.; Bell, A. T. Calibration of the DFT/GGA+U Method for Determination of Reduction Energies for Transition and Rare Earth Metal Oxides of Ti, V, Mo, and Ce. *J. Chem. Theory Comput.* **2011**, *7*, 2218–2223.

(51) Xu, Z.; Rossmeisl, J.; Kitchin, J. R. A Linear Response DFT+U Study of Trends in the Oxygen Evolution Activity of Transition Metal Rutile Dioxides. *J. Phys. Chem. C* **2015**, *119*, 4827–4833.

(52) Zhang, S. B.; Northrup, J. E. Chemical Potential Dependence of Defect Formation Energies in GaAs: Application to Ga Self-Diffusion. *Phys. Rev. Lett.* **1991**, *67*, 2339–2342.

(53) Freysoldt, C.; Grabowski, B.; Hickel, T.; Neugebauer, J.; Kresse, G.; Janotti, A.; Van De Walle, C. G. First-Principles Calculations for Point Defects in Solids. *Rev. Mod. Phys.*

2014, *86*, 253–305.

(54) Makov, G.; Payne, M. Periodic Boundary Conditions in Ab Initio Calculations. *Phys. Rev. B* **1995**, *51*, 4014–4022.

(55) Lany, S.; Zunger, A. Assessment of Correction Methods for the Band-Gap Problem and for Finite-Size Effects in Supercell Defect Calculations: Case Studies for ZnO and GaAs. *Phys. Rev. B* **2008**, *78*, 17–20.

(56) Oba, F.; Togo, A.; Tanuka, I. Defect Energetics in ZnO: A Hybrid Hartree-Fock Density Functional Study. *Phys. Rev. B* **2008**, *77*, 245202.

(57) Broclawik, E.; Haber, J. SCF-SW-Xα Calculations of the Removal of Oxygen from Oxide Surfaces by Vacancy Formation and Crystallographic Shear Mechanisms. *J. Catal.* **1981**, *72*, 379–382.

(58) Gai, P. L.; Boyes, E. D. Electron Microscopy Studies of Catalysis by Oxides. *Electron Microscopy in Heterogeneous Catalysis*; Institute of Physics Publishing: Bristol and Philadelphia, 2003.

(59) Bursill, L. A. Crystallographic Shear in Molybdenum Trioxide. *Proc. R. Soc. Lond. A. Math. Phys. Sci.* **1969**, *311*, 267–290.

(60) Silvi, B.; Savin, A. Classification of Chemical Bonds Based on Topological Analysis of Electron Localization Functions. *Nature* **1994**, *371*, 683–686.

(61) Setyawan, W.; Curtarolo, S. High-Throughput Electronic Band Structure Calculations: Challenges and Tools. *Comput. Mater. Sci.* **2010**, *49*, 299–312.

(62) Anderson, J. S.; Brown, J. M.; Cheetham, A. K.; Dreele, R. V. O. N.; Hutchinson, J. L.; Lincoln, F. J.; Bevan, D. J. M.; Straehle, J. Point Defects and Extended Defects in Niobium Oxides. *Nature* **1973**, *243*, 81–83.

TABLE OF CONTENTS GRAPHIC

For Table of Contents Only

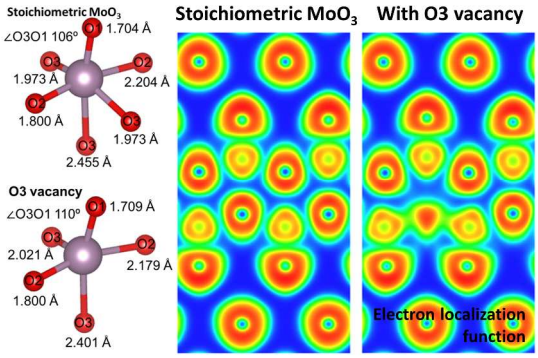

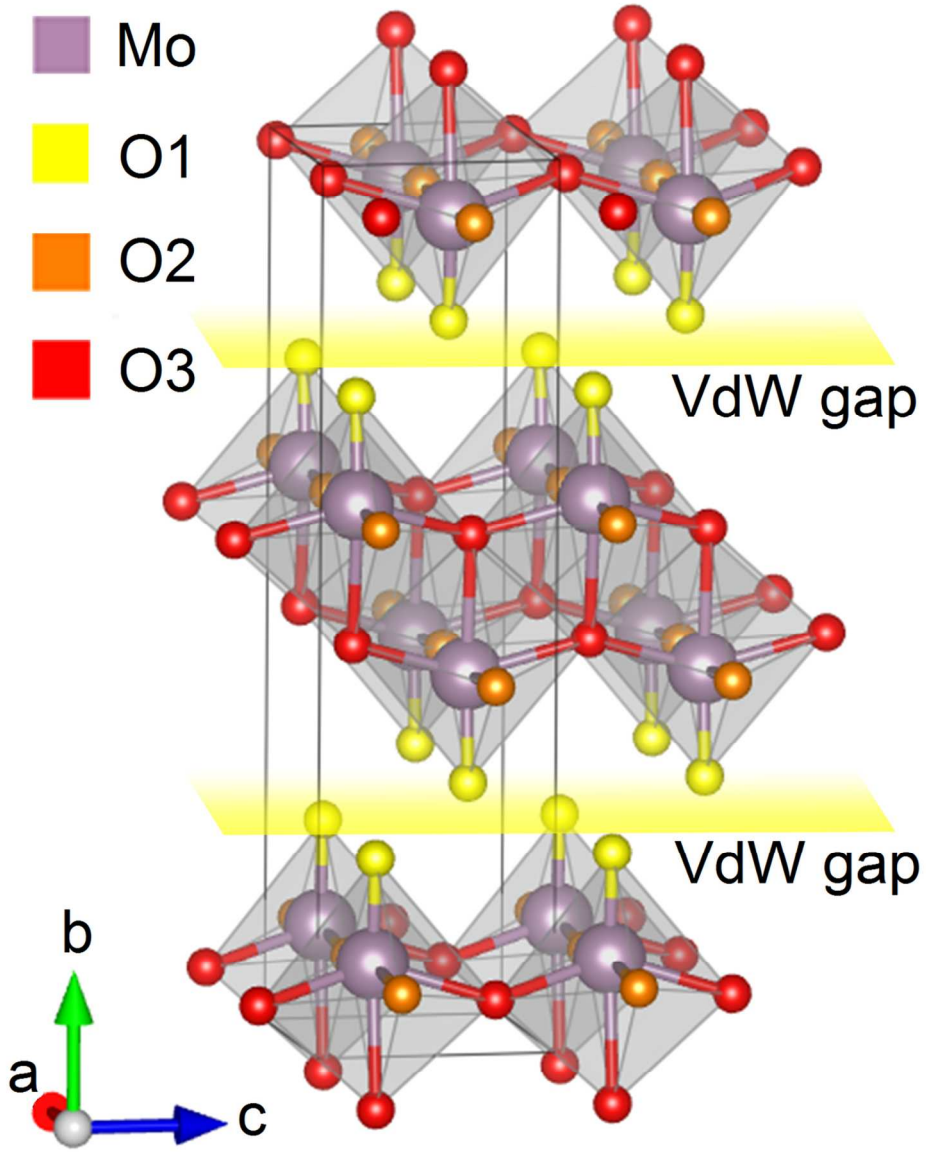

Figure 1. Crystal structure of MoO_3 showing the three inequivalent oxygen positions and the van der Waals gap. O1 is the apical oxygen; O2 is corner-sharing and O3 edge-sharing.
105x133mm (300 x 300 DPI)

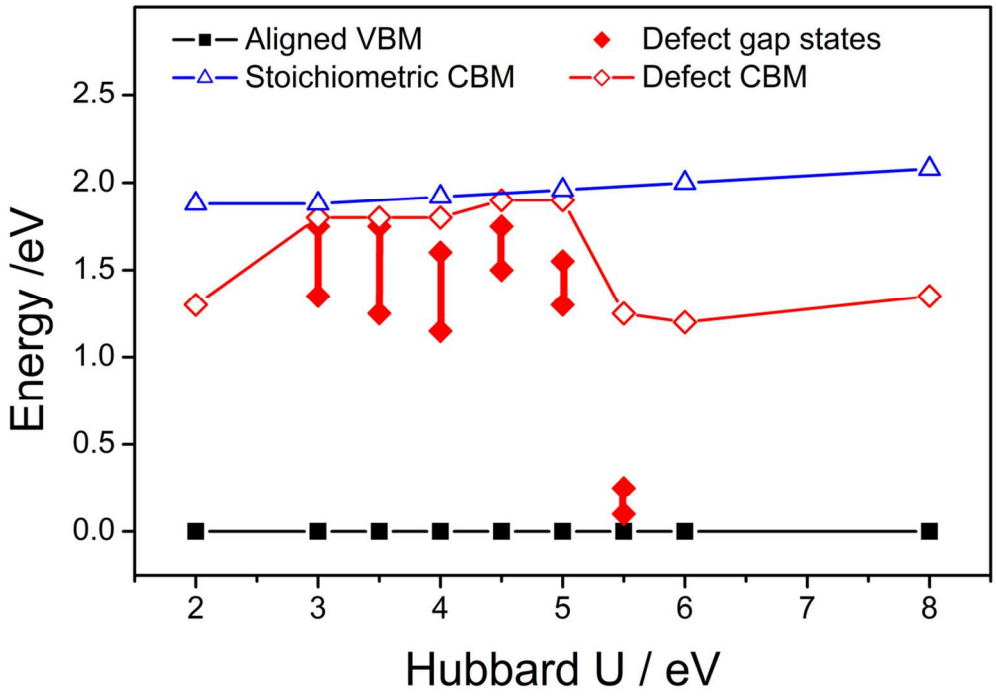

Figure 2. Aligned valence band maximum, stoichiometric conduction band minimum, defect gap states and defect conduction band minimum as a function of U parameter for a 2x1x2 supercell, where the defect is an oxygen vacancy on the O2 position.
57x39mm (600 x 600 DPI)

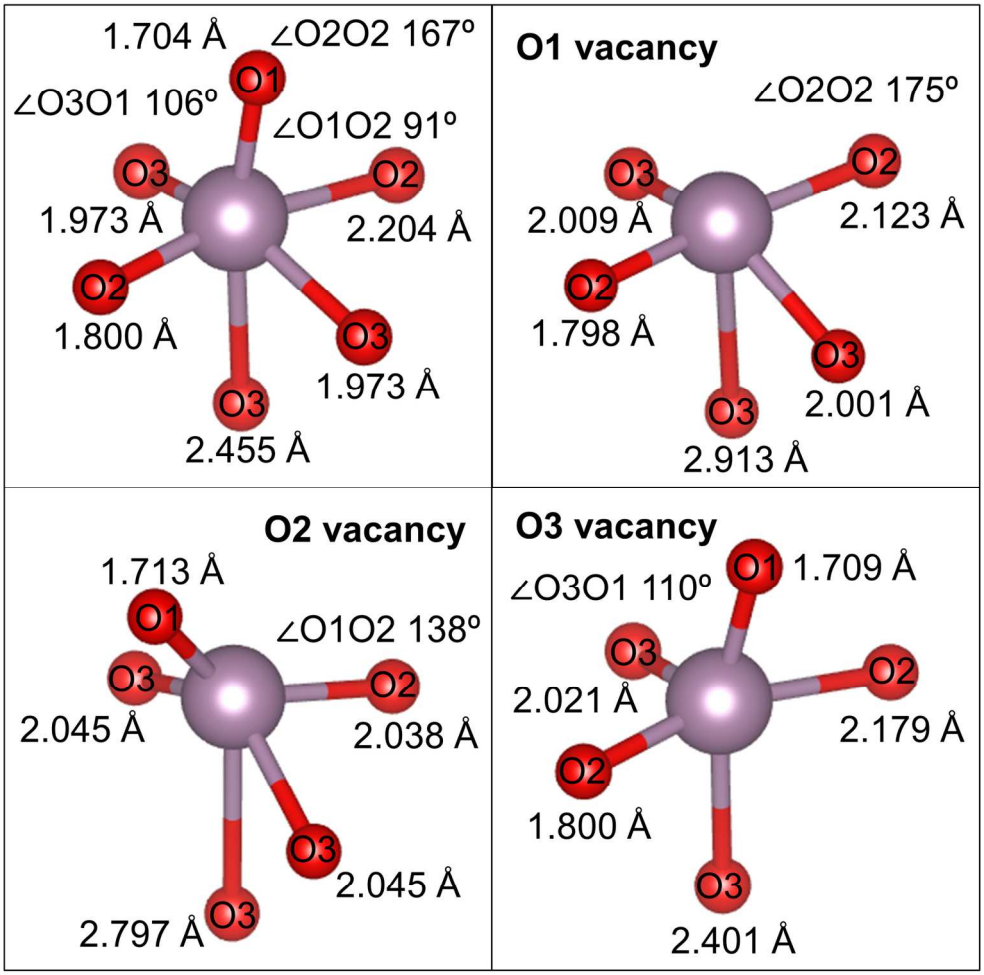

Figure 6. Bond lengths and select bond angles on an octahedron in stoichiometric MoO3, and the distorted polyhedrons adjacent to vacancies on O1, O2, O3 positions. Octahedra are aligned to comparable orientations.
81x80mm (600 x 600 DPI)

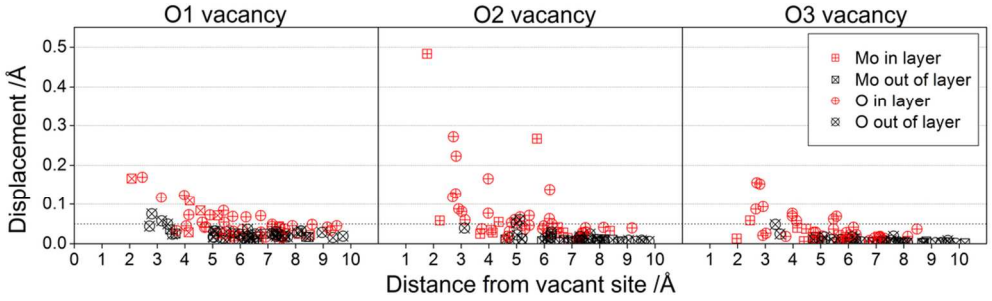

Figure 7. Mo and O ion displacements from stoichiometric position with distance from the vacant site for O1, O2 and O3 vacancy positions in a 3x1x3 (144 atom) supercell. In layer and out of layer signifies if the ion is located within the same layer as the vacancy or not.
51x14mm (600 x 600 DPI)

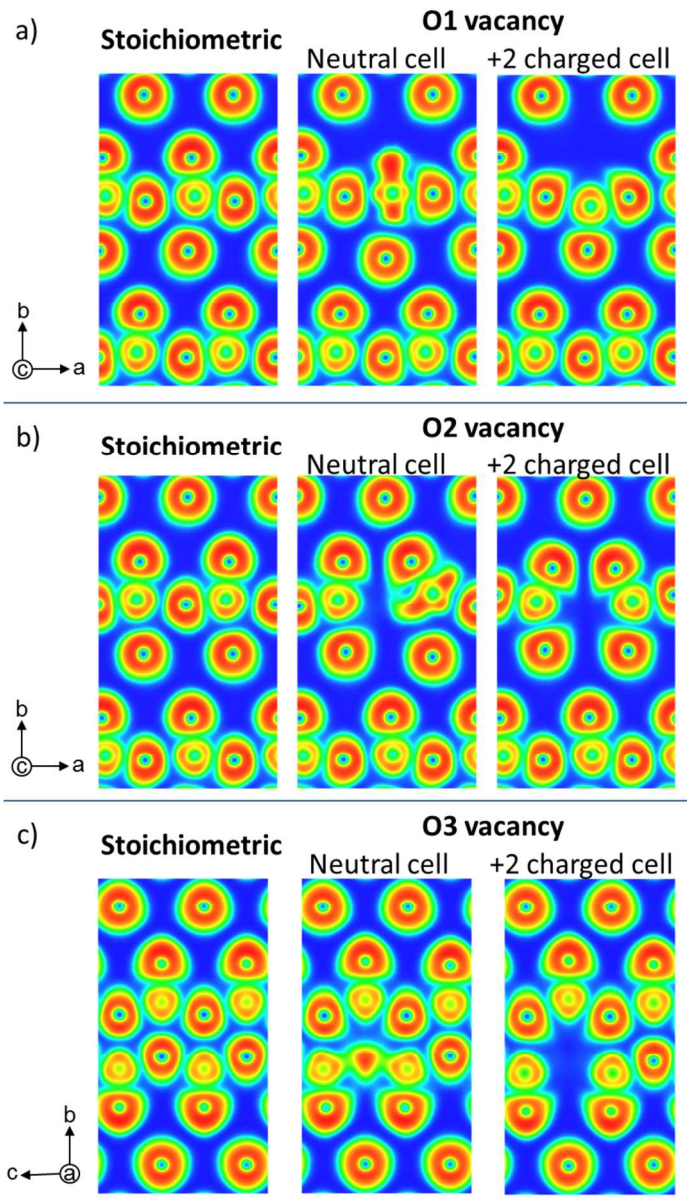

Figure 8. Plots of the electron localization function of 2x1x2 supercells containing a) O1, b) O2 and c) O3 vacancies. The defect cells are shown in neutral and +2 charge states alongside the stoichiometric cell. 126x222mm (300 x 300 DPI)

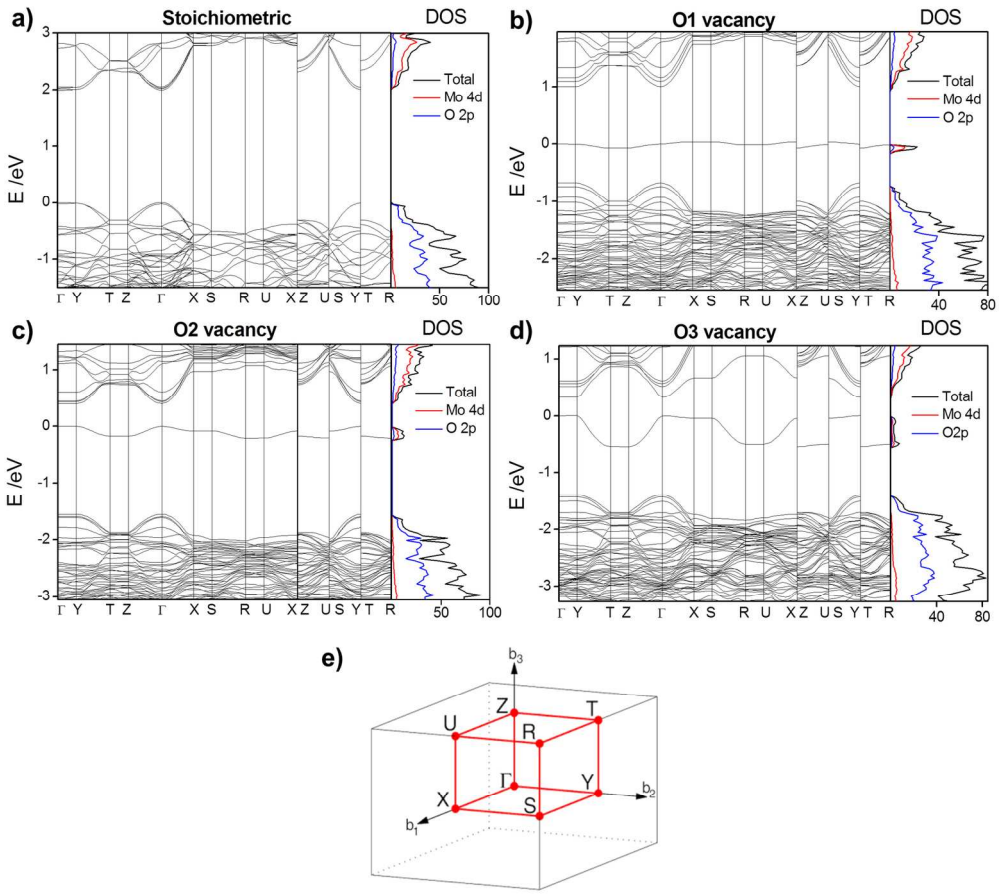

Figure 9. Band structures of MoO3 a) in the stoichiometric case, and with a vacancy on b) O1, c) O2 and d) O3 positions, alongside the total, Mo 4d and O 2p density of states. The Fermi level is aligned to 0 eV. e) Brillouin zone of an orthorhombic lattice.60 The path Γ-Y-T-Z-Γ-X-S-R-U-X|Z-U|S-Y|T-R was used for calculating bandstructures.
159x142mm (300 x 300 DPI)

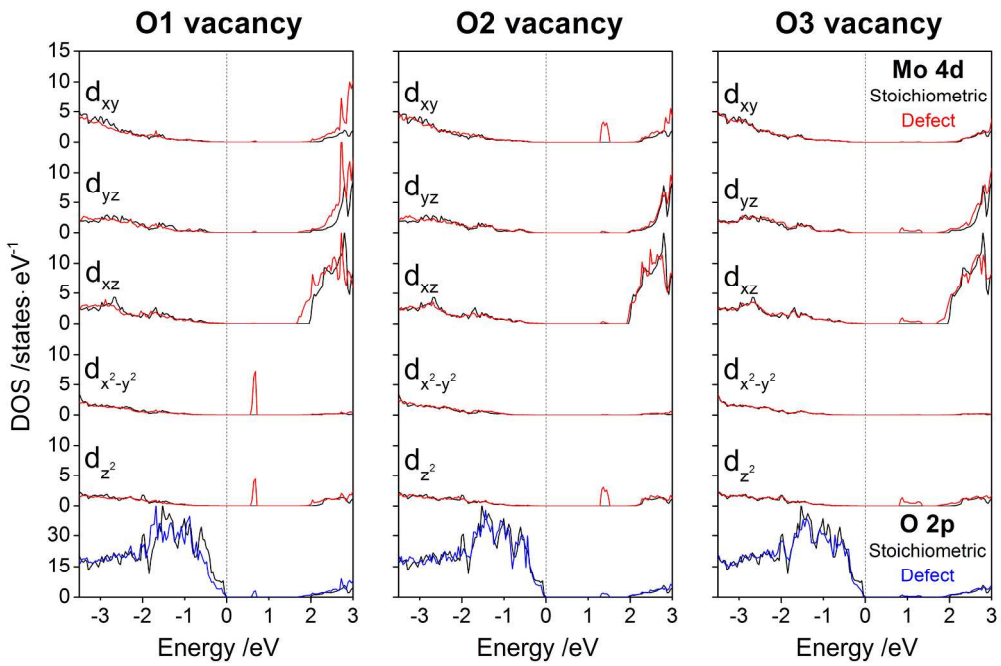

Figure 10. Orbital resolved density of states comparing the stoichiometric and defect Mo 4dxy, 4dyz, 4dxz, 4dx2-y2, 4dz2 and O 2p orbitals, with O1, O2 and O3 vacancies.
117x77mm (600 x 600 DPI)